Journal of Materials Processing Tech. 321 (2023) 118148

Contents lists available at ScienceDirect

Journal of Materials Processing Tech.

journal homepage: www.elsevier.com/locate/jmatprotec

Simulation of metal punching and trimming using minimal experimental characterization

David Gustafsson [a,*], Sergi Parareda [b,c], Laia Ortiz-Membrado [c], Antonio Mateo [c], Emilio Jiménez-Piqué [c], Erik Olsson [a]

[a] Luleå University of Technology, Department of Engineering Sciences and Mathematics, Division of Solid Mechanics, Luleå, 971 87, Sweden
[b] Eurecat, Centre Tecnològic de Catalunya, Unit of Metallic and Ceramic Materials, Manresa, 08243, Spain
[c] CIEFMA, Universitat Politècnica de Catalunya, Barcelona, 08019, Spain

ARTICLE INFO

Associate Editor: Marion Merklein

Keywords:
Punching
Trimming
Shear cutting
Shearing process
FEM simulation

ABSTRACT

This paper presents a validated finite element modeling approach for simulating shear cutting, needing a minimal amount of experimental characterization. Only one uniaxial tensile test and one force–displacement relationship from a punching experiment are needed for calibration, with maintained prediction accuracy compared to more experimentally demanding approaches. A key ingredient is the observation that the Lode angle parameter is close to zero in the fracture region, postulating that the fracture strain only depends on stress triaxiality, with one free calibration parameter. The true stress–strain behavior is provided from inverse modeling of the tensile test, whereas the fracture model is calibrated using the punching test. The model is verified for different materials by comparing force–displacement curves for punching experiments not used in the calibration. The prediction error for the intrusion is below 4%. A validation is made for two setups. The local residual stresses are measured using Focused Ion-Beam Digital Image Correlation (FIB-DIC). The simulated values are within the experimental bounds. Cut edge morphology and plastic strains obtained by nano-indentation mappings are compared to simulation results, showing a decent agreement. For trimming, the cut edge morphology prediction performance decreases at 17% cutting clearance while it is maintained over the whole range for punching. The predicted hardness values have a mean absolute percentage error below 7.5%. Finally, the effect of element size and remeshing is discussed and quantified. The minimal experimental characterization and simulation effort needed, enables an efficient optimization of the cutting process in the industry.

1. Introduction

Shear cutting, such as punching and trimming, of sheet metals is a commonly used process in the automotive and HDV (Heavy-Duty Vehicle) industry for medium to high series production due to low cycle times. The main drawbacks are that the edge properties obtained in shear cutting have an impact on both sheet metal formability, see Pätzold et al. (2023), and fatigue resistance, see Parareda et al. (2023). In the task of weight optimization in the HDV and automotive industries, one important tool is increased material grade. Examples of candidates for this are the complex phase steels CP800 and CP980. A challenge with increased material grades is that the mentioned drawbacks from the shear cutting processes often become more pronounced, as shown by Maronne et al. (2003), and have to be quantified.

As stated already by Brokken et al. (1998), one step towards adequate quantification of these effects is by simulation of the shear cutting process to obtain the residual stresses, the shape, and the hardening state of the cut edge. This is a task including high nonlinearities, large deformations, and crack propagation. Numerous studies have been carried out to increase the understanding of the process and to provide a methodology for quantification of the edge damage. Brokken et al. (2000) used an Operator Split Arbitrary Lagrange Euler (OS-ALE) method to simulate plane strain blanking, using cutting clearances of 0%–10%. Their aim was to predict the cut edge morphology. Despite the ALE mesh description, they found it necessary to apply remeshing to avoid unacceptable mesh distortions. Han et al. (2016) simulated trimming of 1.4 mm ultra-high strength press hardened steel using a cutting clearance (c.cl.) of 5%. Six different failure criteria were calibrated using an iterative process where the trimming tool displacement from experiments was compared to the simulation ditto. The predicted edge morphologies were then compared to the experimental results.

* Corresponding author.
E-mail address: david.gustafsson@ltu.se (D. Gustafsson).

https://doi.org/10.1016/j.jmatprotec.2023.118148
Received 28 June 2023; Received in revised form 17 August 2023; Accepted 3 September 2023
Available online 9 September 2023

It turned out that none of the models were significantly better than the others using these evaluation criteria. They selected the model presented by Oyane et al. (1980) for further evaluation. Han et al. (2022a) studied the damage induced by trimming of 1.6 mm DP780 using the failure criterion presented by Cockcroft and Latham (1968). In another work, Han et al. (2022b) studied trimming of 1.6 mm QP980 comparing six different failure models, concluding that the Cockcroft–Latham criterion was the most competitive. In both studies, the simulation and calibration methodology was similar to the one presented by Han et al. (2016). Hydro-piercing, a process showing a lot of similarities to punching, was studied by Wu et al. (2010). Six ductile fracture criteria were compared and it was concluded that the only model able to show satisfactory agreement with experiments, was the one based on the work by Rice and Tracey (1969). Habibi et al. (2023) simulated punching of 1.5 mm DP1000 using the four parameter failure model presented by Bai and Wierzbicki (2008), varying the calibration constants to explore the effect of fracture loci on edge cracking sensitivity. They found that the stress state in the elements around the cut edge varied in terms of stress triaxiality during the cutting process, but that the normalized Lode angle parameter was kept around 0. This conclusion is strengthened by the work done by Sandin et al. (2022) who simulated punching of 1.5 mm CP1000HD using a five parameter fracture model. They found it difficult to use plane stress specimens for calibration of the fracture loci due to the limited information it provides for stress states of normalized Lode angle parameter being close to zero. For ductile solids, Lode angle parameter zero also seems to provide the lowest failure strains for a given stress triaxiality, as shown by Barsoum and Faleskog (2011). This means that failure models based on a Lode angle parameter range close to zero, should provide conservative results for other stress states. Barsoum and Faleskog (2011) also show that the critical localization strains is increasing with decreased triaxiality over the whole Lode parameter range. Pätzold et al. (2023) designed a two-stage shear cutting simulation model to study how the hardening in the shear affected zone was influenced by different shear cutting parameters. They used the three parameter Johnson Cook fracture criterion and determined the parameters inversely by comparing the geometric characteristics of the simulated cut edges to experiments. The studied material was a dual-phase steel HCT780X of thickness 1.5 mm. In contrast to the earlier mentioned, Pätzold et al. (2023) used remeshing to avoid the heavily distorted mesh that often occur, mainly in the burnish zone. Bai and Wierzbicki (2010) used an extended Mohr–Coulomb criterion with good accuracy in predicting fracture. They state that the shape of the fracture loci at the line represented by Lode angle parameter zero could be captured by a simple exponential function, which is also the form the Rice–Tracey criterion takes in the space of equivalent strain to fracture $\bar{\varepsilon_f}$ and stress triaxiality η.

The highlighted findings, of the mentioned works above, clearly show the possibility to achieve satisfactory shear cutting simulation results using multiple parameter failure models. Many of the available studies are, however, limited to moderate sheet thicknesses, cutting clearances and/or a single material. In addition, the usage of multiple calibration parameters often requires extensive efforts both in terms of simulations and experiments. This complexity could be an obstacle when new materials and process parameters are examined in the industry.

The aim with this work is to enhance the possibilities for innovation, by providing a simplified and industry feasible simulation approach. An approach that is valid for a wide range of shear cutting processes, materials, sheet thicknesses and process parameters. It is shown that a standard tensile test for calibration of the flow-curve, and a punching test for calibration of a single parameter failure model, is enough to capture the key characteristics of the cut edge for both punching and trimming of multiple sheet thicknesses and cutting clearances. The approach is verified and validated by studies of punch force–displacement results, cut edge morphologies, residual stresses and hardness in the shear affected zone.

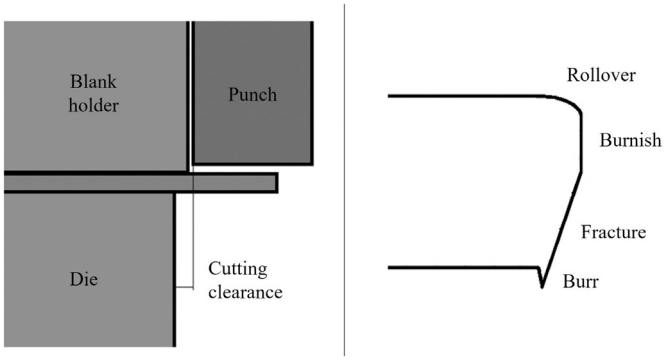

Fig. 1. Schematic sketches of a shear cutting setup (left) and a cut edge (right).

2. Theory

Following the reasoning of Bai and Wierzbicki (2010), the failure strain could be interpreted as a surface uniquely dependent of the stress triaxiality η and the Lode angle parameter $\bar{\Theta}$. In this work the stress triaxiality η is defined by

$$\eta = \frac{\sigma_m}{\bar{\sigma}} \tag{1}$$

where σ_m is the hydrostatic stress

$$\sigma_m = \frac{1}{3}(\sigma_1 + \sigma_2 + \sigma_3) \tag{2}$$

and $\bar{\sigma}$ is the von Mises stress

$$\bar{\sigma} = \sqrt{\frac{1}{2}\left[(\sigma_1 - \sigma_2)^2 + (\sigma_2 - \sigma_3)^2 + (\sigma_3 - \sigma_1)^2\right]}. \tag{3}$$

with σ_1, σ_2 and σ_3 being the principal stresses. The Lode angle Θ ranges from 0 to $\pi/3$ in the deviatoric plane and is defined by

$$\cos(3\theta) = \frac{27(\sigma_1 - \sigma_m)(\sigma_2 - \sigma_m)(\sigma_3 - \sigma_m)}{2\bar{\sigma}^3}. \tag{4}$$

As shown by Bai and Wierzbicki (2010), a normalization of θ to obtain a range of -1 to 1 yields the Lode angle parameter $\bar{\Theta}$ such that

$$\bar{\Theta} = 1 - \frac{6}{\pi}\theta. \tag{5}$$

A schematic sketch of a shear cutting setup is presented in Fig. 1 together with a sketch of a typical cut edge where the different zones are pointed out according to VDI 2906-2:1994 (1994). These zones will be referred to later in this work. The cutting clearance is defined as the horizontal distance between the punch and die, expressed as a percentage of the sheet thickness.

3. Approach

As stated earlier, and which will be further proved later in this work, the Lode angle parameter $\bar{\Theta}$ plays a subordinate role in simulation of shear cutting processes. Hence, finding a function describing equivalent strain to fracture $\bar{\varepsilon}_f$ as a function of stress triaxiality η alone, could be sufficient for accurate simulations of shear cutting processes. Based on the findings presented above this function can be assumed to take the shape

$$\bar{\varepsilon}_f = C_1 \exp(C_2 \eta) \tag{6}$$

where C_1 and C_2 are calibration parameters for a given material and also, which is sometimes overlooked, for a given element size in finite element analyses. With two or more calibration parameters the risk of finding a so-called local optimum in the calibration process increases. For a given shear cutting configuration, multiple combinations of C_1 and C_2 could yield satisfying results. One possibility to minimize this

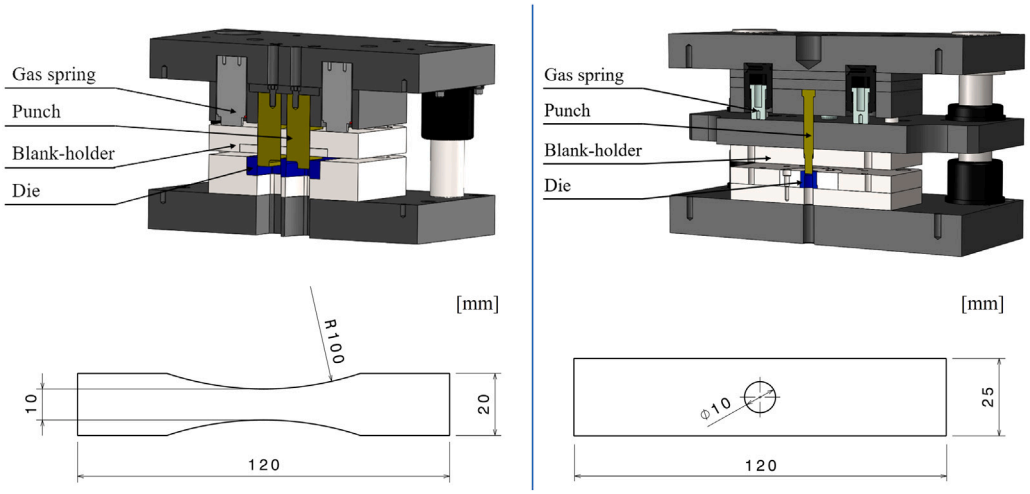

Fig. 2. Trimming tools and geometry of trimmed specimens (left). Punching tools and geometry of punched specimens (right).

risk is to use a calibration process where multiple shear cutting parameters, e.g. cutting clearances, are evaluated simultaneously and the pair of constants that yields the minimum weighted error is selected. To avoid this somewhat complicated process it is tempting to make the assumption that C_2 could be assigned a value that is valid for a wide range of materials. This would leave only one calibration parameter and a single, global optimum can easily be found for a given material and mesh size. In the major part of the mentioned studies above, where different fracture loci has been compared, a value of $C_2 = 1.5$ has been used. This is in line with the original work by Rice and Tracey (1969) even though they were focusing on non-hardening materials. Wu et al. (2010) tried other values of this parameter, but found 1.5 being the most suitable. In this work, the fracture loci are hence assumed to be described by the equation

$$\bar{\varepsilon}_f = C\exp(1.5\eta) \tag{7}$$

for all studied materials, covering different types of metals and material grades. The calibration parameter C is calibrated for a single punching configuration for each material minimizing the difference between punch force–displacement curves obtained from simulations and experiments. The results are verified comparing punch force–displacement curves obtained from simulations and experiments for other cutting clearances and material sheet thicknesses. To validate the simulation approach, the cut edge morphology is studied for both punching (closed cut) and trimming (open cut). Nano-indentation and residual stress measurements are used for further validation.

To model the material behavior before fracture, isotropic von-Mises plasticity is assumed. The hardening functions are calibrated against standard (DIN EN ISO 6892-1:2019, 2019) tensile tests results in terms of engineering stress–strain curves. Normally this procedure is used up to necking because of the mesh dependency after localization. By using a very fine mesh this mesh dependency can be avoided. The motivation for this possibility is that the localization shape directly follows from the hardening history during the tensile test. The importance of accurately modeling the flow stress behavior after necking is further discussed later.

4. Materials and methods

4.1. Studied materials and configurations

Three different materials were studied, one aluminum alloy and two complex phase steels, in the configurations presented in Table 1. For each material one configuration was selected for calibration of the failure model described by Eq. (7). These calibration points are punching of CP800, CP980 and AA6082-T6 in the thicknesses 3.4, 3.5 and 2.0 mm, with cutting clearances 8.8, 8.5 and 15%, respectively.

Table 1
Studied configurations. Punched and trimmed specimens with different sheet thicknesses t and cutting clearances $c.cl$. Failure model calibration configurations in bold.

Material	VDA-code	t [mm]	Trimmed c.cl. [%]	Punched c.cl. [%]
CP800	HR660Y760T-CP	3.4	8.8	–
			17.6	–
			–	**8.8**
CP980	HR780Y980T-CP-SF	3.5	8.5	–
			–	**8.5**
			17.0	–
			–	24.1
AA6082-T6		2.0	–	**15.0**
		5.0	–	6.0

The punched and trimmed specimen shapes, which are presented in Fig. 2 with the corresponding tools, were produced quasi-statically in a servo-hydraulic machine. The tools are assumed to be rigid in this analysis. The punching setup features a load measuring device in the top of the punch to accurately monitor the force during cutting.

The chemical composition of the studied materials according to the material suppliers are presented in Table 2, and the mechanical properties in Table 3.

4.2. Measurement of cut edge morphology and residual stresses

To validate the simulation model, the simulated cut edge morphologies and residual stresses were compared to experimental measurements. The cut edge morphologies, represented by black lines in Fig. 11, were obtained using a 3D profilometer Alicona InifiniteFocusSL equipped with a 10x objective.

The residual stress measurements were performed at the cut edges using a method called Focused Ion Beam-Digital Image Correlation (FIB-DIC), see Lord et al. (2018). Punched specimens of CP980 with cutting clearances of both 8.5% and 24.1% were studied. A cut-out was made in the specimens according to Fig. 3, resulting in a smaller part, see Fig. 4, that could be mounted in a scanning electron microscope (SEM).

The FIB-DIC methodology can be summarized in the steps: (i) Initial SEM imaging; (ii) Milling of the determined shape using FIB, (iii) SEM imaging; (iv) Strain relief measurement using DIC; (v) Calculation of residual stresses.

Table 2
Chemical composition of the studied materials (wt.%). Maximum content presented for the steels.

Mtrl.	Fe	C	Si	Mn	P	S	Al	Cu	B	Ti + Nb	Cr + Mo	–
CP800	Bal.	0.18	1.0	2.2	0.05	0.01	1.2	0.2	0.01	0.25	1.0	–
CP980	Bal.	0.20	1.0	2.2	0.05	0.01	1.2	0.2	0.01	0.25	1.0	–
Mtrl.	Fe	Mg	Si	Mn	Pb	Zn	Al	Cu	Ca	Cd	Ti	Cr
AA6082	0.37	0.85	0.97	0.54	0.00	0.02	97.1	0.03	0.00	0.00	0.04	0.01

Table 3
Mechanical properties in transverse direction of the studied materials in terms of yield stress $R_{p0.2}$, Tensile strength R_m and elongation A_{50}.

Mtrl.	$R_{p0.2}$ [MPa]	R_m [MPa]	A_{50} [%]
HR CP800 SF	778	835	16.5
HR CP980 SF	957	1034	12.8
AA6082 T6	298	333	12.9

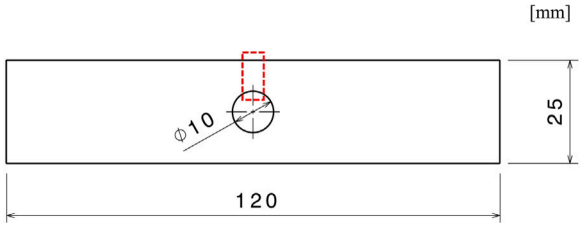

Fig. 3. Cutout zone in punched specimen.

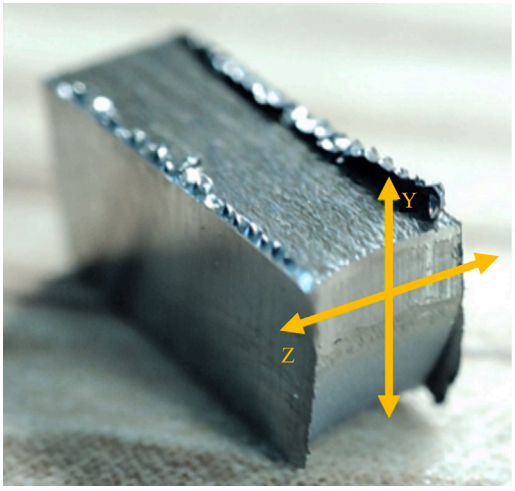

Fig. 4. Part to be mounted in the SEM.

A thin layer of platinum was applied before the initial milling and a surface pattern, necessary for the DIC measurements, was created using FIB. For the milling a ring-core geometry, see Fig. 5, was selected. This consisted of a ring with an inner diameter of 10 μm, milled in five steps using a current of 440 pA up to a depth of 10 μm. The FIB was a Carl Zeiss Neon40 Crossbeam operated at 30 kV. Displacements were measured at each step and recalculated to strains. The residual stresses σ_{zz} in the z-direction (see Fig. 5) were calculated using the equation

$$\sigma_{zz} = -\frac{E}{1-\nu^2}[\Delta\varepsilon_{\infty}^{zz} + \nu\Delta\varepsilon_{\infty}^{yy}] \tag{8}$$

where $\Delta\varepsilon^{zz}$ and $\Delta\varepsilon^{yy}$ are the measured strains in the respective directions.

4.3. Nano-indentation measurements

High-speed nanoindentation, see Besharatloo et al. (2020) for a more detailed description of the method, was used to evaluate the

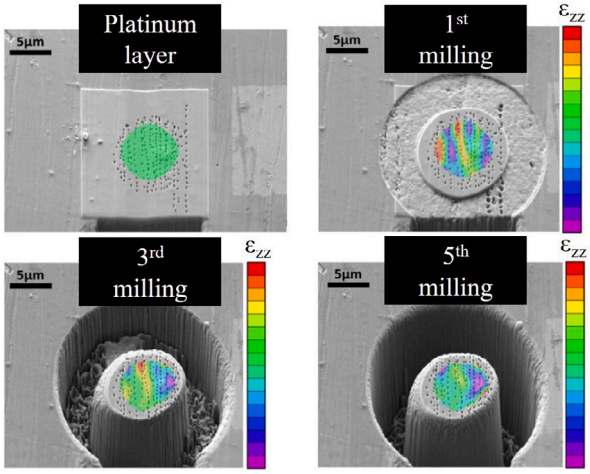

Fig. 5. Ring-core milling for residual stress measurements.

cut edge hardness increase in two of the configurations presented in Table 1, the punched CP980 using cutting clearances 8.5% and 24.1%. The measurements and mappings were performed using diamond Berkovich indenter by applying a force of 2 mN. The distance between the indentation points were 1.6 μm, considering the work performed by Besharatloo and Wheeler (2021). The size of the maps were 200 × 400 μm^2.

This data could then be compared with simulation results through a recalculation from effective plastic strains to hardness. This recalculation is made by assuming a linear relationship between the hardness H and the yield stress at 8% plastic strain σ_{y8} such that

$$H = k\sigma_{y8} \tag{9}$$

where k can be estimated if the hardness as well as the stress–strain relationship is known for the base material, as shown by Tabor (1951). According to Nix and Gao (1998) this parameter value is around three for an infinitely large indentation, but is expected to be lower for smaller indentations due to gradient effects.

5. Finite element simulation

5.1. Simulation setup

The finite element simulations are performed in LS-Dyna R13.1.0 SMP using explicit time integration. 2D plane strain elements are used for the open cut simulations and axisymmetric solid volume weighted elements for the closed cut ditto. Only 4-node under-integrated elements are used. R-adaptive remeshing, based on the work by Dick and Harris (1992), is utilized to accommodate for the large local plastic deformations which can lead to mesh distortions. At the remeshing steps a completely new mesh is constructed for the blank using with four node elements of size 0.02 mm. This element size is in line with the works of Pätzold et al. (2023) using 0.0035 mm × 0.021 mm, Han et al. (2016) using 0.01 mm × 0.02 mm and Habibi et al. (2023) using 0.025 mm × 0.025 mm × 0.025 mm. The tools, die and blank holders are modeled as rigid bodies with edge radius 0.03 mm which lies in

Table 4
Power law parameters after calibration.

Material	A [MPa]	B [MPa]	n [–]	B_{pn} [MPa]	n_{pn} [–]
CP800	765	585	0.60	520	0.45
CP980	840	470	0.22	470	0.22
AA6082-T6	292	250	0.50	250	0.26

Table 5
Calibrated failure model parameter for the studied materials.

Constant	CP800	CP980	AA6082-T6
C [–]	2.5	3.0	0.9

between measured values of 0.01–0.033 mm, and which is the smallest size that can be resolved by the selected blank mesh size. Habibi et al. (2023) used an edge radius of 0.05 mm and Han et al. (2022a) used 0.02 mm. For the aluminum alloy the elastic modulus and Poisson's ratio are 70 GPa and 0.33, as used by Rong et al. (2021), respectively. The corresponding values used for the steels are 200 GPa and 0.3, as used by Sun et al. (2017). The elastic moduli were computed using the initial slope of the uniaxial tensile tests. A constant Coulomb friction model coefficient of 0.1 is used for the contact interfaces in accordance with Wang et al. (2015). Naturally, full large deformation theory is relied upon in the analysis.

5.2. Material flow stress modeling

To model the plastic flow stress σ behavior until necking, a elasto-plastic material model is used where the true stress σ to true plastic strain ε_p relationship reads

$$\sigma = A + B\varepsilon_p^n. \tag{10}$$

A, B and n is calibrated to fit the experimental stress–strain data. Thermal, damage and strain rate effects are ignored. The calibration is made using a simple four node shell element model and the results are then applied to a detailed three-dimensional model to evaluate the behavior after necking. In case the simulation and experiment data diverge, the calibration parameters B and n are adjusted for the post-necking part of the curve (B_{pn}, n_{pn}), until satisfactory agreement is achieved. The resulting parameters are presented in Table 4. The elastic region is governed by the elastic modulus and Poisson's ratio. The engineering stress–strain data for both simulations and experiments is presented in Fig. 6. The true stress–strain data serving as input to the flow stress material model is presented in Fig. 7. For strains above 1 a linear extrapolation using the last slope of the curve is utilized. The simulation results for the engineering stress strains curves are retrieved from simulations using the calibrated failure models. The under-predictions of the failure strains in the tensile tests are expected. As mentioned earlier, Barsoum and Faleskog (2011) show that the failure surface has a minimum along the line where the Lode angle parameter is zero, whereas in a standard uniaxial tensile test, the corresponding theoretical value is one.

5.3. Material failure modeling

The failure criterion is implemented using a generalized, incremental, stress state dependent damage model (GISSMO) in LS-Dyna. A damage parameter D is used in an uncoupled manner. In this case *uncoupled* means that there is no degradation of the material load bearing capacity or stiffness before rupture. D is only used for bookkeeping. For undamaged material $D = 0$ and failure occur at $D = 1$, leading to erosion of the actual element. The damage is accumulated non-linearly with the damage increment $\dot{D}$ described by

$$\dot{D} = \frac{2\sqrt{D}}{\bar{\varepsilon}_f}\dot{\varepsilon}_p \tag{11}$$

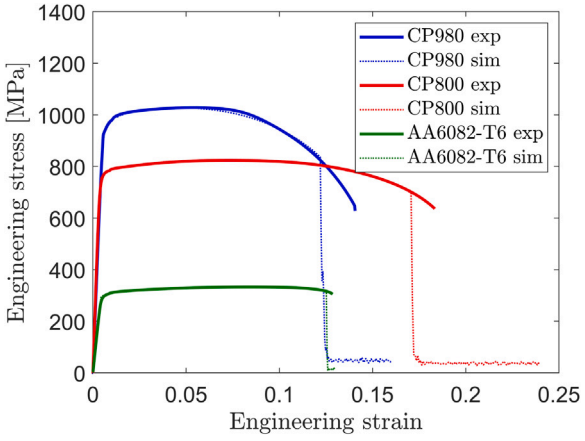

Fig. 6. Engineering stress–strain data for AA6082-T6 (A80), CP800 (A50) and CP980 (A50).

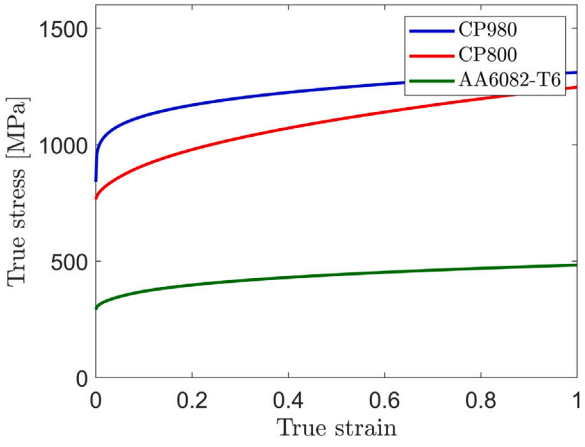

Fig. 7. True stress–strain input for flow stress material model.

where $\dot{\varepsilon}_p$ is the equivalent plastic strain increment, and the equivalent strain to fracture $\bar{\varepsilon}_f$ is calculated according to Eq. (7). The calibrated parameter C of Eq. (7) is presented in Table 5 for the studied materials. The resulting fracture loci are shown in Fig. 8.

6. Results and discussion

6.1. Relevant lode angle parameter range

As mentioned above, Habibi et al. (2023) found that the Lode angle parameter was close to zero during the whole process of punching. However, they studied a relatively thin sheet of 1.5 mm thickness, with a moderate cutting clearance of 13.3% of the sheet thickness, and a relatively large punch diameter of approximately 20 times the sheet thickness. A common rule of thumb for the minimum possible punch diameter is around 1–1.5 the sheet thickness. Approaching this limit is not uncommon in industry and sometimes is even overruled in the HDV industry where sheet thicknesses can approach 10 mm. For example, Stahl et al. (2020), who studied punching in relation to fatigue strength of truck frame parts, selected a sheet thickness of 8 mm and a punch diameter of around 15 mm. At these material

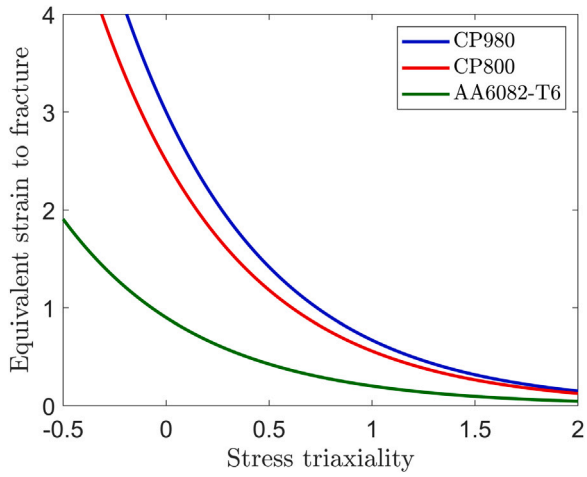

Fig. 8. Calibrated failure locus for the studied materials.

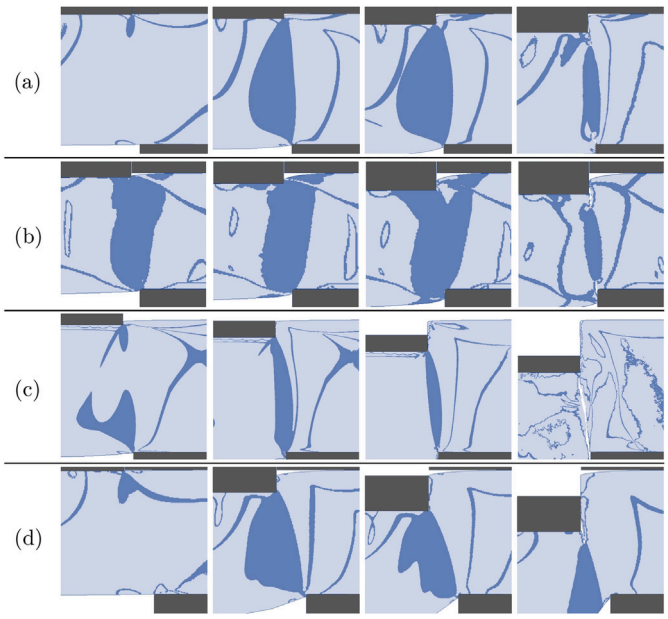

Fig. 9. Lode angle parameter during the shear cutting process. The darker areas contain a Lode angle parameter between −0.06 and 0.06. (a) punching (d = 10 mm) of 5 mm AA6082-T6 with c.cl. 6%; (b) trimming of 2 mm AA6082-T6 with c.cl. 7.5%; (c) punching (d = 10 mm without blank holder) of 8 mm CP800 with c.cl 8.0%; (d) punching (d = 10 mm) of 3.52 mm CP980 with c.cl. 24.1%.

thicknesses, the usage of a blank holder is sometimes disregarded in series production, which might affect the stress state.

To further validate the path of only focusing on Lode angle parameter zero a more comprehensive study of the subject is presented below. A sheet thickness range of 2–8 mm, cutting clearances of 6–24.1%, punch diameter d to sheet thickness t factors of 1.25–5 and all the studied materials are covered. The possible difference in Lode angle parameter during cutting between an open and closed cut process is also studied. In Fig. 9, fringe plots of the Lode angle parameter are presented with areas containing values of −0.06 to 0.06 being represented by dark blue and all other values by light blue. The total range for this parameter is −1 to 1. During the whole cutting process the Lode angle parameter in the designated crack path stays within a narrow Lode angle parameter range around zero. This is true both for trimming and punching, and a wide range of process parameters.

6.2. Failure model calibration and verification

Comparing Figs. 6 and 8 is evident that the failure loci are not directly linked to the failure strains seen in a tensile test. The tensile test of CP800 shows significantly larger strains before failure as compared to CP980. Still, the failure loci for CP980 are located higher than the CP800 ditto. One explanation for this could be found in Fig. 7, where it is shown that CP800 exhibit more hardening. The increased hardening leads to decreased localization of the deformation. This makes it possible for CP800 to accommodate larger strains globally before fracture, even though the local strains before fracture are smaller than for CP980. From the engineering stress–strain curve of AA6082-T6, shown in Fig. 6, it seems like the curve after necking is relatively short. The small post-necking strain indicate that when the material gets localized deformations, total fracture is close. This is also reflected in the low values of the failure model loci as compared to the studied steels.

The resulting punch force–displacement curves for the open cut configurations presented in Table 1, are presented in Fig. 10. The calibration configurations are marked with bold lines and dots. The lines represent the simulation results and the dots experimental data. It is evident that a failure model that is calibrated for a small cutting clearance, following the presented approach, can predict the process response in terms of punch force and displacement for a significantly larger cutting clearance. When the failure model calibration is done for a relatively thin material of 2 mm it could predict the shear cutting process response for a thick sheet of 5 mm. It is also evident that process data can be captured for a wide range of materials, in this case yield stresses ranging from approximately 300 to 950 MPa.

6.3. Validation

To validate the model, the resulting cut edge morphologies, residual stresses and hardness profiles have been studied.

The simulated and measured cut edge morphologies are compared in Fig. 11 for a number of different configurations. The edges exhibit distinct zones resulting from the shearing process as presented schematically in Fig. 1: the rollover, burnish, fracture and, in one case, burr zone. Despite utilizing the same material and thickness, the shape of the punched edges differs significantly. In the case of around 9% clearance, approximately one-third of the edge thickness is attributed to the burnish zone, while the remaining two-thirds belong to the fracture zone. On the contrary, for clearances of 17.0% and 24.1%, the rollover and fracture angles become more prominent in the edge profile. Regarding trimming using large cutting clearances, a tendency of overpredicting the height of the rollover zone, at cost of the burnish height, is evident. The height of the fracture zone remains accurately predicted. As shown in Fig. 13, and by Shiozaki et al. (2015) the most critical zone is the fracture zone due to large tensile residual stresses. It can also be mentioned that the cutting clearances in question are above the common industrial range.

As shown by for example Shiozaki et al. (2015), the residual stresses can vary from relatively high compression to high tensile values along the cut edge. For thick materials, and for cut edges where the height of the different zones are evenly spread, this local variation could probably be captured by X-ray diffraction where the measurement area could be around 1 mm in diameter, as stated by Shiozaki et al. (2015). To get more local information for validation, the FIB-DIC method described earlier was selected in this work.

The ability to capture the 2D stress state was the primary factor in the selection of the ring-core geometry. According to Korsunsky et al. (2010), the technique allows for the analysis of strain relief in the core from various angles due to its isotropic milling geometry, providing a quantitative measurement of the full 2D in-plane stress state within the sample under investigation. The ring-core method has an advantage

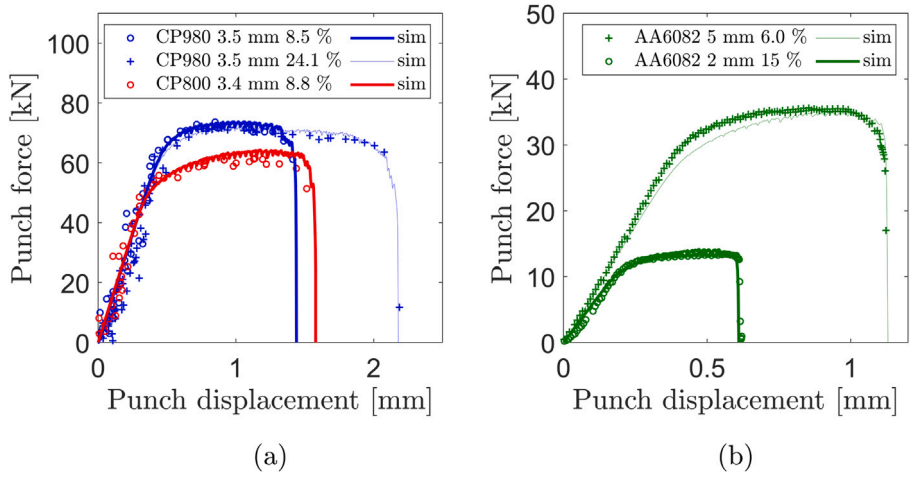

Fig. 10. Punch force–displacement curves for punching of (a) CP980 and CP800; (b) AA6082-T6. Dots for experimental data and lines for simulation results. Calibration configurations in bold.

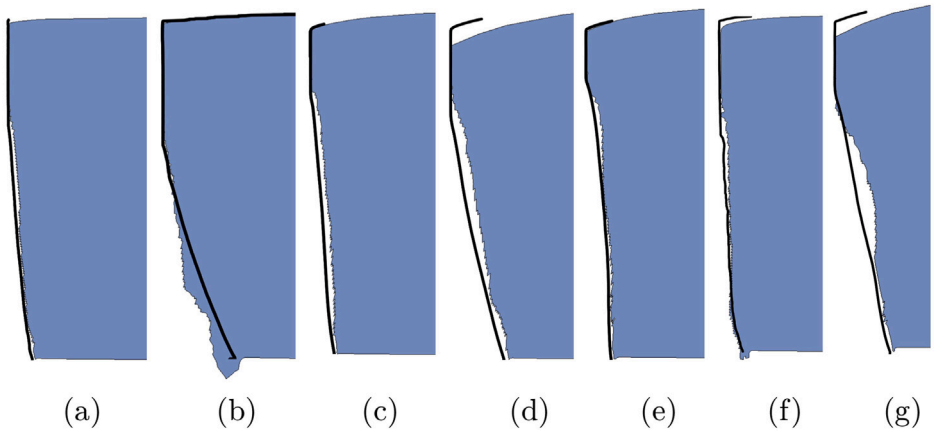

Fig. 11. Comparison of cut edge morphologies obtained from simulations and experiments (bold line). (a) Punching of 3.52 mm CP980 c.cl. 8.5%; (b) Punching of 3.52 mm CP980 c.cl. 24.1%; (c) Trimming of 3.52 mm CP980 c.cl. 8.5%; (d) Trimming of 3.52 mm CP980 c.cl. 17.0%; (e) Trimming of 3.4 mm CP800 c.cl. 8.8%; (f) Punching of 3.4 mm CP800 c.cl. 8.8%; (g) Trimming of 3.4 mm CP800 c.cl. 17.6%.

over other techniques like micro-scale hole drilling and micro-slotting because the core generally shows more strain relief, which increases resilience against noise.

Additionally, the largely consistent strain relief throughout the middle of the core makes it easier to average effectively and improves interpretational robustness in accordance with the suggestions by Lord et al. (2018). Multiple milling stages and pictures were used to improve the strain estimation accuracy, in contrast to the direct comparison between only two sets of SEM images collected before and after milling, even if the DIC approach could have limits regarding the measured area size.

It is important to note that this technique is particularly suitable for getting useful data from a non-planar, limited-area surface, despite monitoring a confined area that may not be entirely typical of the full fracture surface. Due to restrictions on surface shape and size, methods like X-ray may not offer similar insights.

The adaptability of the ring-core shape is shown by its use in studies involving damaged regions, supporting its usefulness in a variety of study contexts. Somov et al. (2022) used it for residual stress measurements in a shot peened titanium alloy. Sebastiani et al. (2015) went for the same shape in their study of dental veneering ceramics. Salvati et al. (2016) used the ring-core shape to obtain local information about residual stresses studying the overload effect in fatigue. However, while noting the inherent flaws in any measuring approach, required measures were taken to mitigate and account for these effects. Some artifacts may still appear in the data.

Table 6
Residual stress in lower half of shear zone of punched CP980. Cutting clearance 8.5% and 24.1%. Minimum values presented for simulations.

Cutting clearance [%]	Exp. [MPa]	Sim. [MPa]
8.5	165 ± 226	−20
24.1	−618 ± 97	−620

The positions for the residual stress measurements are presented in Fig. 12. Corresponding fringe plots are shown in Fig. 13. The resulting stress levels are presented in Table 6.

It is evident that the simulation model is able to both qualitatively and quantitatively distinguish between the two cutting clearances. However, while both presented results are within the experimental margin of error, the result for 8.5% is closer to the limit. As seen in Fig. 13, the simulated stress gradient in the transition zone between burnish and fracture, is higher for the lower cutting clearance as compared to 24.1%. The stress increases from values around zero to high positive values, over a relatively short distance. This makes the selection of the simulation evaluation area more critical, which might explain the discrepancy. Due to the high gradients and the very local measurement data, the exactness and value of the residual stress validation can be discussed. The results are promising, but a

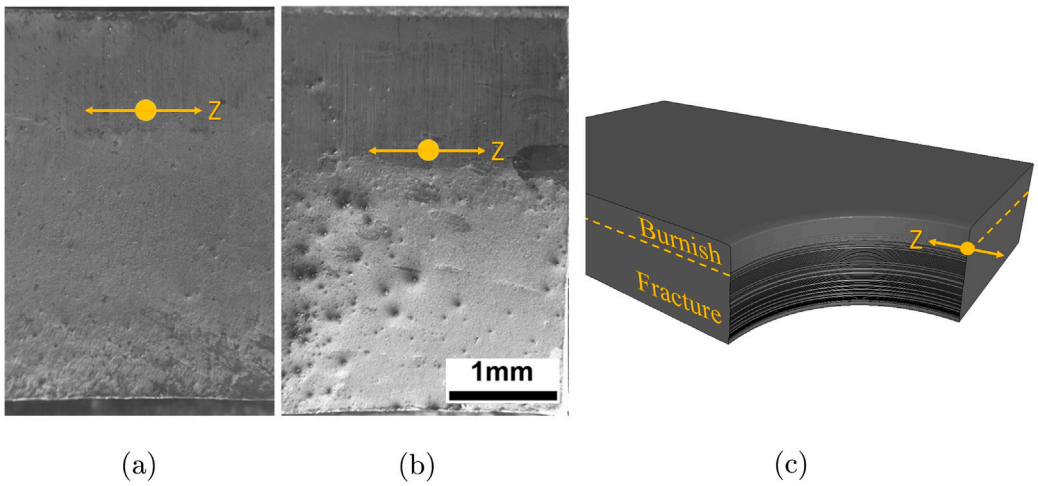

Fig. 12. Approximate residual stress measurement position and direction for punched CP980 3.52 mm. (a) Cutting clearance 8.5%; (b) Cutting clearance 24.1%; (c) 3D illustration of a quarter of a punched hole, including the residual stress measurement position.

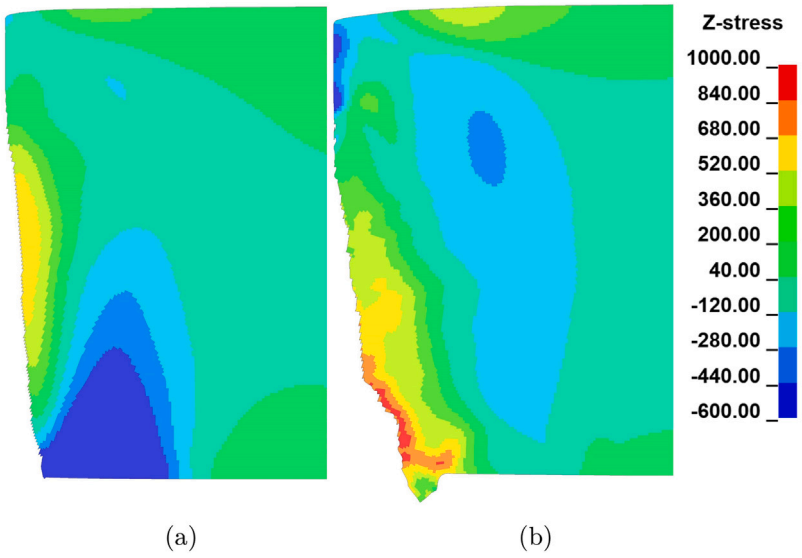

Fig. 13. Fringe plot of residual stresses in Z-direction. Punching of CP980 3.52 mm using a c.cl. of (a) 8.5%; (b) 24.1%.

full field evaluation of the stress field would undoubtedly provide further insight. The ability to capture residual stresses from shear cutting processes could be useful in predicting for example fatigue resistance where the residual stress has a major influence, see for example Dehmani et al. (2018).

The high-speed nanoindentation maps containing results of the hardness measurements are presented in Figs. 14 and 15 along with fringe plots of the effective plastic strains obtained in simulations. In Figs. 16 and 17 the hardness values in the different cut edge zones of punched CP980 (cutting clearance 8.5% and 24.1%) are given for experiments and simulations, respectively. The corresponding Mean Absolute Percentage Errors (MAPE) are also presented for each figure. The simulation results show good agreement both in a qualitative sense, where the effective plastic strain field is compared to the hardness measurement field, and quantitatively, when the effective plastic strains are recalculated to hardness using Eq. (9). For CP980 the parameter k in this equation was calculated to a value of 3.94. The largest average error, MAPE 7.49%, is found in the burnish zone using cutting clearance 8.5%. The largest percentage error for a single point, 15.72%, is found using the same cutting clearance but in the fracture zone (lwr), close to the surface, see Fig. 16(c).

6.4. Flow curve sensitivity

The blank experiences very high local strains during cutting. Because of this, the flow curve shape and magnitude, even at strains far above necking, could have an impact on the final results. Hence, the calibrated failure model is tied to a specific material flow model. In Fig. 18 two different material model inputs are presented in (a), and their impact on simulation of an ordinary tensile test is presented in (b). As shown in Fig. 18(a), the material model input diverge at true strains above 30%, a difference that is less pronounced in the ordinary tensile test simulation. Fig. 19 suggest that the process response, in terms of punch force–displacement curve, is sensitive to this type of input difference making it a suitable tool for calibration of the failure surface, whereas the difference in cut edge morphology is much more subtle. It is also clear that barely visible differences in an ordinary tensile test could be manifested clearly in a punch-force displacement response.

The response from ordinary tensile tests, performed in the same direction and from the same material batch, could have a potentially larger variation than the example shown in Fig. 18, and the variations

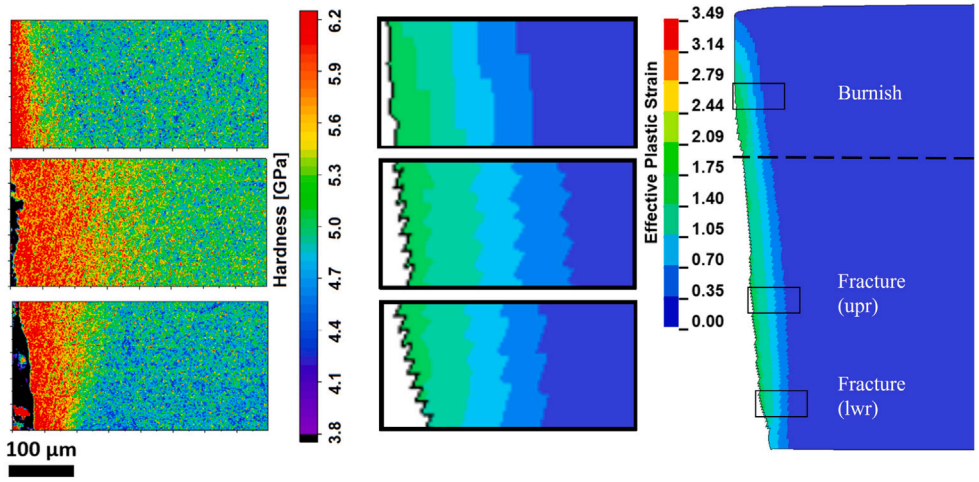

Fig. 14. High-speed nanoindentation maps along with effective plastic strain field from corresponding simulation of punched CP980 using a c.cl. of 8.5%.

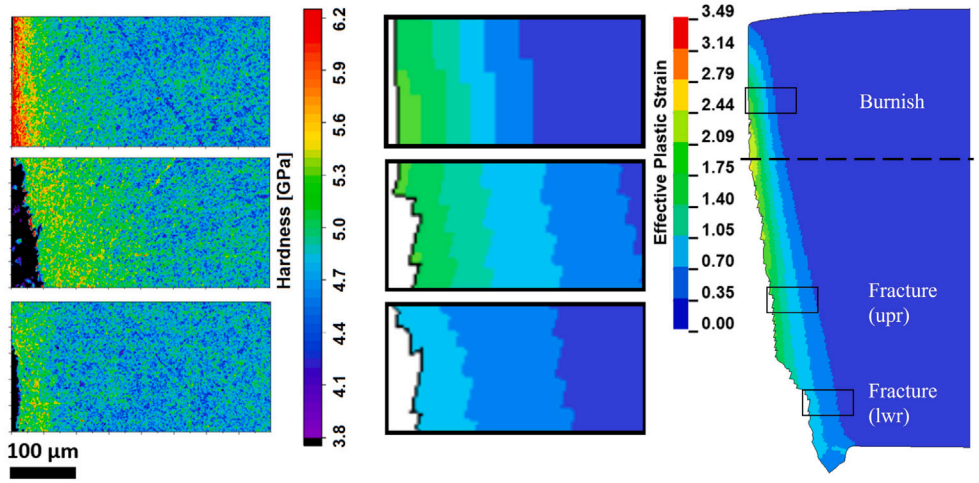

Fig. 15. High-speed nanoindentation maps along with effective plastic strain field from corresponding simulation of punched CP980 using a c.cl. of 24.1%.

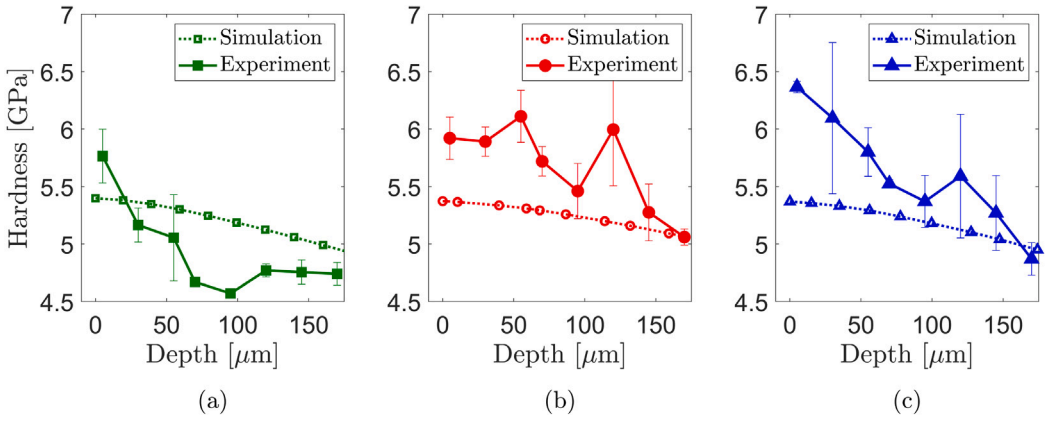

Fig. 16. Measured and simulated hardness of in the different cut edge zones punched CP980 using c.cl. 8.5%. (a) Burnish zone, MAPE 7.49%; (b) Fracture zone (upr), MAPE 7.44%; (c) Fracture zone (lwr), MAPE 7.45%.

between different directions could be significant even for materials that are normally assumed to be isotropic. During punching, all directions between the sheet rolling direction and the transverse direction are represented along the hole perimeter. Hence, there is no surprise that the cut edge morphology will vary. A two-dimensional approach, like the one presented in this work, could capture this variation by performing e.g. a Monte Carlo analysis where the material model input parameters are varied. But it can also be used with fixed material

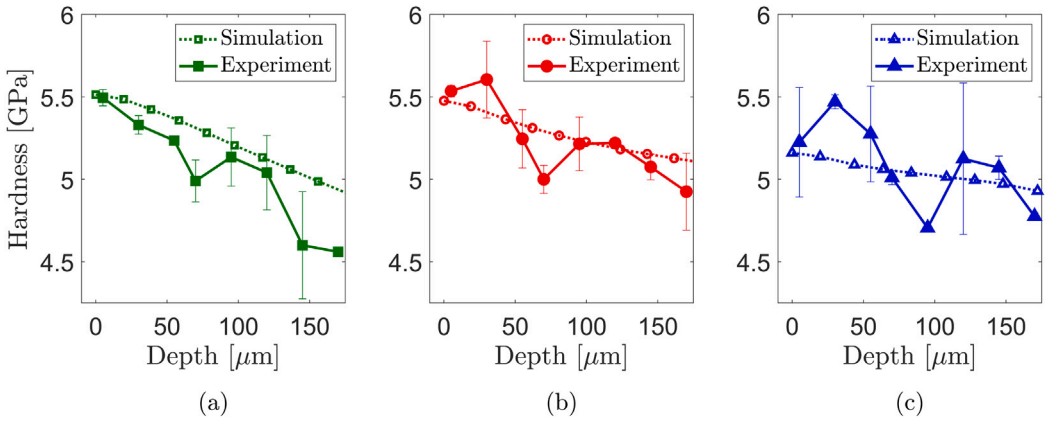

Fig. 17. Measured and simulated hardness of in the different cut edge zones punched CP980 using c.cl. 24.1%. (a) Burnish zone, MAPE 4.03%; (b) Fracture zone (upr), MAPE 2.32%; (c) Fracture zone (lwr), MAPE 3.37%.

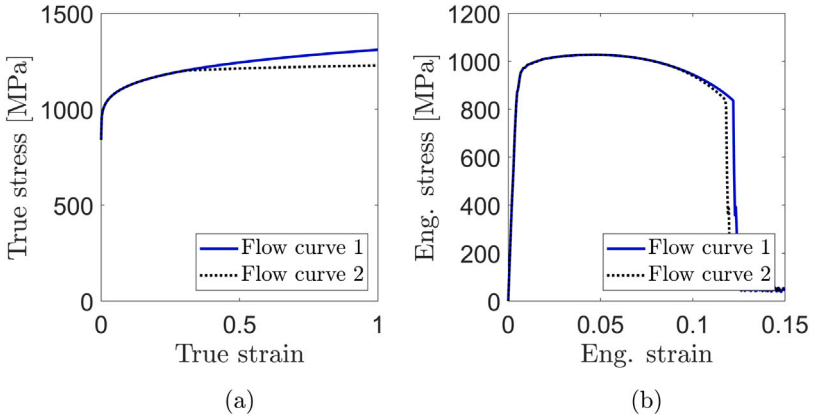

Fig. 18. (a) Different true stress–strain flow curves for the material model; (b) Engineering stress–strain flow curves, obtained from simulation of uniaxial tensile test.

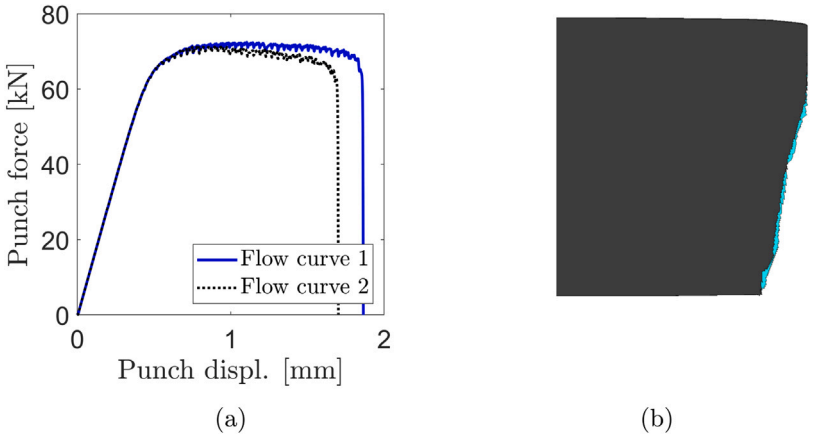

Fig. 19. Material model flow curve effect on (a) process response; (b) cut edge morphology, where cyan represent results using flow curve 1, and black flow curve 2. Punching of 3.52 mm CP980 using a c.cl. of 17%.

flow and failure model to compare the impact of different process parameters on hardening, residual stresses, cut edge morphology, etc.

6.5. Mesh dependency

As mentioned earlier, failure models that are based on equivalent strain to fracture has an inherent element size dependency. This is illustrated by Fig. 20(a) where the punch force–displacement response for 2 mm aluminum is compared for two different characteristic element lengths l and two remeshing intervals i. This dependency can to some extent be reduced, see 20(b), by using a scale function that scales the failure locus depending on element size. For the application of punching and trimming this is superfluous since the same mesh size will work for most different configurations. In this example a linear scale function is used so that the scale factor s is described by

$$s = -10l + 1.2. \tag{12}$$

The benefit of using remeshing is most evident for relatively large cutting clearances. This is illustrated in Fig. 21 where the cut edge

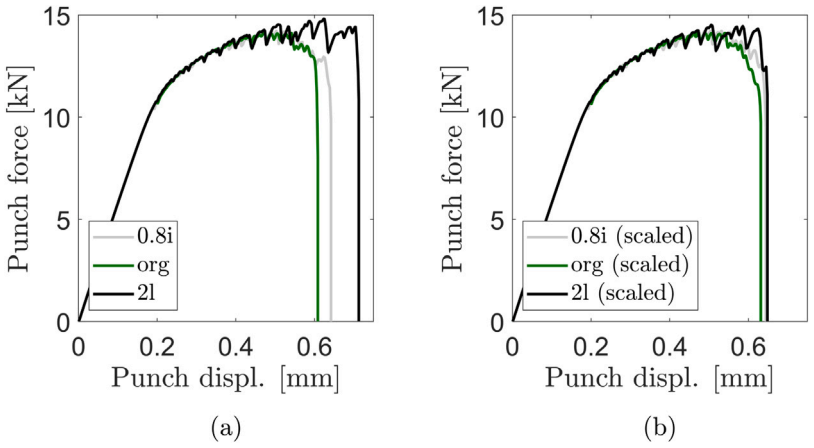

Fig. 20. Mesh dependency in punching simulation of 2 mm AA6082-T6 (c.cl. 15%) using failure model calibration parameter C = 0.9. (a) Without scaling; (b) With scaling. The reference cases *org* use a remeshing interval *i* and mesh size *l*. This is compared to a shorter remeshing interval *0.8i* and to a larger mesh *2l*.

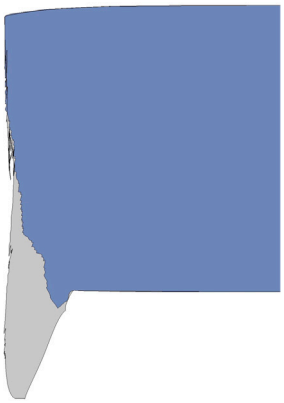

Fig. 21. Cut edge morphology obtained from simulations using remeshing (blue) and without remeshing (gray). Punching of 3.52 mm CP980 using a cutting clearance of 24.1%. (For interpretation of the references to color in this figure legend, the reader is referred to the web version of this article.)

morphologies obtained with and without remeshing are compared. For the non-remeshing simulation, the element size in the critical region was set according to suggestion by Han et al. (2016), 0.01 mm × 0.02 mm.

7. Conclusions

A simple numerical approach for predicting residual stresses and cut edge morphology based on finite elements is presented in this paper. The ability to make these predictions in a convenient manner could potentially be of great importance in studies of process parameters and material selection. Especially when put in a context of fatigue life and crack initiation point assessment, and formability prediction of punched or trimmed components. Putting this work into such a context in the future could further prove the usefulness of the results. There is also room for further increase of simulation efficiency by applying remeshing and mesh refinement locally in the designated crack path. The main conclusions from this study are:

- The Lode angle is close to zero in the fracture zone at shear cutting allowing for a failure model only dependent on the stress triaxiality.
- The stress triaxiality dependency on fracture in a shear cutting context, could be described by an expression using only one calibration parameter, for widely different metals.
- Two experiments for calibration of the simulation material model are enough to achieve satisfactory results in terms of cut edge morphology, residual stresses and hardness for a wide range of configurations.
- The failure curve/surface can be scaled using a mesh size dependent function. This reduces effects of both different mesh sizes and remeshing intervals.
- The benefits of using a strategy, e.g. remeshing or another mesh description than Lagrangian, to handle the large local mesh deformation increases with increased cutting clearance.
- Differences in simulation input are more clearly manifested in the punch force–displacement curve, than in the tensile test engineering stress–strain curve or the cut edge morphology. This suggest that the force–displacement curve is a better optimization parameter in material model calibration than the other two.
- The strain at fracture in a standard uniaxial tensile test does not correlate with fracture strain in the material failure model. This means that a seemingly more ductile material could have a lower local ductility, which clearly manifest in processes with forced local deformation, such as shear cutting.

CRediT authorship contribution statement

David Gustafsson: Conceptualization, Methodology, Investigation, Validation, Formal analysis, Writing – original draft. **Sergi Parareda:** Writing – original draft, Investigation. **Laia Ortiz-Membrado:** Writing – original draft, Investigation, Formal analysis. **Antonio Mateo:** Writing – review & editing, Supervision, Funding acquisition. **Emilio Jiménez-Piqué:** Writing – review & editing, Supervision. **Erik Olsson:** Writing – review & editing, Supervision, Project administration.

Declaration of competing interest

The authors declare that they have no known competing financial interests or personal relationships that could have appeared to influence the work reported in this paper.

Data availability

Data will be made available on request.

Acknowledgments

The authors would like to thank ArcelorMittal and Centro Ricerche Fiat for providing test materials and material data for this study, and the European Union for providing funding of the Fatigue4Light project (Horizon 2020, LC-GV-06-2020 project no. 101006844) in which this study was conducted. Grant PID 2021-126614OB-I00 funded by MCIN/AEI/10.13039/501100011033 and the European Union NextGenerationEU/PRTR are also acknowledged. Special thanks to Olle Sandin and Daniel Casellas for providing a solid simulation model base to build upon. The authors are also grateful to the Direcció General de Recerca del Comissionat per a Universitats i Recerca de la Generalitat de Catalunya for recognizing CIEFMA as a consolidated Research Group (2021SGR01053).

References

Bai, Y., Wierzbicki, T., 2008. A new model of metal plasticity and fracture with pressure and Lode dependence. Int. J. Plast. 24, 1071–1096. http://dx.doi.org/10.1016/J.IJPLAS.2007.09.004.

Bai, Y., Wierzbicki, T., 2010. Application of extended Mohr-Coulomb criterion to ductile fracture. Int. J. Fract. 161, 1–20. http://dx.doi.org/10.1007/S10704-009-9422-8/METRICS, URL: https://link.springer.com/article/10.1007/s10704-009-9422-8.

Barsoum, I., Faleskog, J., 2011. Micromechanical analysis on the influence of the Lode parameter on void growth and coalescence. Int. J. Solids Struct. 48, 925–938. http://dx.doi.org/10.1016/J.IJSOLSTR.2010.11.028.

Besharatloo, H., Carpio, M., Cabrera, J.M., Mateo, A.M., Fargas, G., Wheeler, J.M., Roa, J.J., Llanes, L., 2020. Novel mechanical characterization of austenite and ferrite phases within duplex stainless steel. Metals 2020 10, 1352. http://dx.doi.org/10.3390/MET10101352, URL: https://www.mdpi.com/2075-4701/10/10/1352.

Besharatloo, H., Wheeler, J.M., 2021. Influence of indentation size and spacing on statistical phase analysis via high-speed nanoindentation mapping of metal alloys. J. Mater. Res. 36, 2198–2212. http://dx.doi.org/10.1557/S43578-021-00214-5/FIGURES/7, URL: https://link.springer.com/article/10.1557/s43578-021-00214-5.

Brokken, D., Brekelmans, W.A., Baaijens, F.P., 1998. Numerical modelling of the metal blanking process. J. Mater Process. Technol. 83, 192–199. http://dx.doi.org/10.1016/S0924-0136(98)00062-4.

Brokken, D., Brekelmans, W.A., Baaijens, F.P., 2000. Predicting the shape of blanked products: a finite element approach. J. Mater Process. Technol. 103, 51–56. http://dx.doi.org/10.1016/S0924-0136(00)00418-0.

Cockcroft, M.G., Latham, D.J., 1968. Ductility and the workability of metals. J. Met. 96, 33–39.

Dehmani, H., Brugger, C., Palin-Luc, T., Mareau, C., Koechlin, S., 2018. High cycle fatigue strength assessment methodology considering punching effects. Procedia Eng. 213, 691–698. http://dx.doi.org/10.1016/J.PROENG.2018.02.065.

Dick, R.E., Harris, W.E., 1992. Fully automatic rezoning of evolving problems. In: Numerical Methods in Industrial Forming Processes.

DIN EN ISO 6892-1:2019, Metallic materials - Tensile testing - Part 1: Method of test at room temperature.

Habibi, N., Zhou, M., Lian, J., Koenemann, M., Muenstermann, S., 2023. Numerical investigation into effects of fracture behavior on edge cracking sensitivity. J. Mater Process. Technol. 316, 117965. http://dx.doi.org/10.1016/J.JMATPROTEC.2023.117965.

Han, S., Chang, Y., Wang, C.Y., Dong, H., 2022a. A comprehensive investigation on the damage induced by the shearing process in DP780 steel. J. Mater Process. Technol. 299, 117377. http://dx.doi.org/10.1016/J.JMATPROTEC.2021.117377.

Han, S., Chang, Y., Wang, C., Han, Y., Dong, H., 2022b. Experimental and numerical investigations on the damage induced in the shearing process for QP980 steel. Materials 15, 3254. http://dx.doi.org/10.3390/MA15093254, 2022, Vol. 15, Page 3254, URL: https://www.mdpi.com/1996-1944/15/9/3254.

Han, X., Yang, K., Ding, Y., Tan, S., Chen, J., 2016. Numerical and experimental investigations on mechanical trimming process for hot stamped ultra-high strength parts. J. Mater Process. Technol. 234, 158–168. http://dx.doi.org/10.1016/J.JMATPROTEC.2016.03.025.

Korsunsky, A.M., Sebastiani, M., Bemporad, E., 2010. Residual stress evaluation at the micrometer scale: Analysis of thin coatings by FIB milling and digital image correlation. Surf. Coat. Technol. 205, 2393–2403. http://dx.doi.org/10.1016/J.SURFCOAT.2010.09.033.

Lord, J., Cox, D., Ratzke, A., Sebastiani, M., Korsunsky, A., Salvati, E., Mughal, M.Z., Bemporad, E., 2018. A Good Practice Guide for Measuring Residual Stresses Using FIB-DIC, Vol. 143. The National Physical Laboratory.

Maronne, E., Galtier, A., Robert, J.-L., Ishikawa, T., 2003. Cutting process influence on fatigue steel sheets properties. WIT Trans. Eng. Sci. 40, 508. http://dx.doi.org/10.2495/FDM030021.

Nix, W.D., Gao, H., 1998. Indentation size effects in crystalline materials: A law for strain gradient plasticity. J. Mech. Phys. Solids 46, 411–425. http://dx.doi.org/10.1016/S0022-5096(97)00086-0.

Oyane, M., Sato, T., Okimoto, K., Shima, S., 1980. Criteria for ductile fracture and their applications. J. Mech. Work. Technol. 4, 65–81. http://dx.doi.org/10.1016/0378-3804(80)90006-6.

Parareda, S., Frómeta, D., Casellas, D., Sieurin, H., Mateo, A., 2023. Understanding the fatigue notch sensitivity of high-strength steels through fracture toughness. Metals 2023 13, 1117. http://dx.doi.org/10.3390/MET13061117, URL: https://www.mdpi.com/2075-4701/13/6/1117.

Pätzold, I., Stahl, J., Golle, R., Volk, W., 2023. Reducing the shear affected zone to improve the edge formability using a two-stage shear cutting simulation. J. Mater Process. Technol. 313, 117872. http://dx.doi.org/10.1016/J.JMATPROTEC.2023.117872.

Rice, J.R., Tracey, D.M., 1969. On the ductile enlargement of voids in triaxial stress fields. J. Mech. Phys. Solids 17, 201–217. http://dx.doi.org/10.1016/0022-5096(69)90033-7.

Rong, Q., Shi, Z., Li, Y., Lin, J., 2021. Constitutive modelling and its application to stress-relaxation age forming of AA6082 with elastic and plastic loadings. J. Mater Process. Technol. 295, 117168. http://dx.doi.org/10.1016/J.JMATPROTEC.2021.117168.

Salvati, E., O'Connor, S., Sui, T., Nowell, D., Korsunsky, A.M., 2016. A study of overload effect on fatigue crack propagation using EBSD, FIB–DIC and FEM methods. Eng. Fract. Mech. 167, 210–223. http://dx.doi.org/10.1016/J.ENGFRACMECH.2016.04.034.

Sandin, O., Hammarberg, S., Parareda, S., Frómeta, D., Casellas, D., Jonsén, P., 2022. Prediction of sheared edge characteristics of advanced high strength steel. In: IOP Conference Series: Materials Science and Engineering, Vol. 1238. IOP Publishing, 012034. http://dx.doi.org/10.1088/1757-899X/1238/1/012034.

Sebastiani, M., Massimi, F., Merlati, G., Bemporad, E., 2015. Residual micro-stress distributions in heat-pressed ceramic on zirconia and porcelain-fused to metal systems: Analysis by FIB–DIC ring-core method and correlation with fracture toughness. Dent. Mater. 31, 1396–1405. http://dx.doi.org/10.1016/J.DENTAL.2015.08.158.

Shiozaki, T., Tamai, Y., Urabe, T., 2015. Effect of residual stresses on fatigue strength of high strength steel sheets with punched holes. Int. J. Fatigue 80, 324–331. http://dx.doi.org/10.1016/J.IJFATIGUE.2015.06.018.

Somov, P.A., Statnik, E.S., Kan, Y., Pisarev, V.S., Eleonsky, S.I., Ozherelkov, D.Y., Salimon, A.I., 2022. FIB-DIC residual stress evaluation in shot peened VT6 alloy validated by X-ray diffraction and laser speckle interferometry. Nanomaterials 12, 1235. http://dx.doi.org/10.3390/NANO12071235, 2022, Vol. 12, Page 1235, URL: https://www.mdpi.com/2079-4991/12/7/1235.

Stahl, J., Pätzold, I., Golle, R., Sunderkötter, C., Sieurin, H., Volk, W., 2020. Effect of one- And two-stage shear cutting on the fatigue strength of truck frame parts. J. Manuf. Mater. Process. 4, http://dx.doi.org/10.3390/JMMP4020052.

Sun, Y., Li, Y., Daniel, W.J., Meehan, P.A., Liu, Z., Ding, S., 2017. Longitudinal strain development in Chain-die forming AHSS products: Analytical modelling, finite element analysis and experimental verification. J. Mater Process. Technol. 243, 322–334. http://dx.doi.org/10.1016/J.JMATPROTEC.2016.12.019.

Tabor, D., 1951. The Hardness of Metals. Oxford University Press.

VDI 2906-2:1994, Quality of cut faces of (sheet) metal parts after cutting, blanking, trimming or piercing; shearing, form of sheared edge and characteristic values. Association of german engineers, engl. VDI-gesellschaft produktion und logistik.

Wang, K., Greve, L., Wierzbicki, T., 2015. FE simulation of edge fracture considering pre-damage from blanking process. Int. J. Solids Struct. 71, 206–218. http://dx.doi.org/10.1016/J.IJSOLSTR.2015.06.023.

Wu, Z., Li, S., Zhang, W., Wang, W., 2010. Ductile fracture simulation of hydropiercing process based on various criteria in 3D modeling. Mater. Des. 31, 3661–3671. http://dx.doi.org/10.1016/J.MATDES.2010.02.046.